Wideband Metasurface Polarization Converter with Double-Square-Shaped Patch Elements

Takashi Noishiki, Ryuji Kuse, and Takeshi Fukusako[*]

Abstract—In this paper, a wideband metasurface reflector that converts plane wave polarization to cross polarization with a double-square-shaped unit cell is proposed, and the principle of polarization conversion based on polarization synthesis is presented. The proposed structure has a unit cell with a longest dimension of 0.37 wavelengths, a width of 0.23 wavelengths, and a thickness of about 0.09 wavelengths. Using this structure, 95% or more of the incident wave power is converted to cross polarization, covering a fractional bandwidth of 32.4% at 8.5 GHz.

1. INTRODUCTION

A metasurface (MS) is an engineered structure on which metallic unit cells are arranged periodically in a planar shape. Such structures can have artificial magnetic conductor (AMC) characteristics with an in-phase reflection coefficient at a certain frequency [1]. Many studies on AMCs have been conducted for realizing low-profile antennas [2] and extending the bandwidth [3]. AMCs have been applied to expand the impedance bandwidth [3, 4]. In addition to the AMC characteristics, the AR bandwidth can be extended with a MS that converts linear polarization (LP) to CP [5–7] in the off-band for 3-dB AR. Conversion techniques of polarization to cross polarization [8–15] and from LP to CP [16–22] have been extensively studied. For example, the principle of the structure in [9] to convert LP to the cross-polarization was explained based on a cut-wire resonator.

Polarization behavior can be explained based on the linear synthesis of two orthogonal basis components of polarization. To present a typical example based on this concept, this paper comprehensively studies a principle proposed for wideband polarization conversion based on the generation principle of CP using perturbation in an MS. The results can contribute to the development of wideband polarization conversion using design techniques for wideband CP antenna. In the proposed structure, the unit cell of the metasurface polarization converter (MSPC) has a double-square-shaped (DSS) patch element on a dielectric substrate with a backing conductor (BC). This structure is essentially based on the same principle as that of a CP antenna with perturbation. The simulated performance of an MSPC of finite size is compared with the measurement results for an MSPC of finite size using unit cell analysis. Finally, the principle of wideband polarization conversion is discussed based on electromagnetic behavior. The results show that the combination of the DSS patch element and the BC yields wideband polarization conversion.

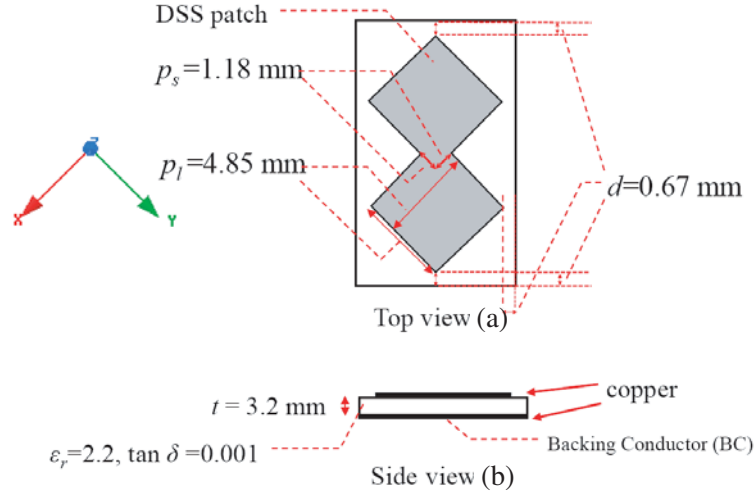## 2. REFLECTION CHARACTERISTICS OF MSPC OF INFINITE SIZE

Figures 1(a) and 1(b) show the top view and side view of the unit cell of the MS, respectively. The unit cell has a DSS patch element, which consists of two square metallic elements, 4.85 mm on a side,

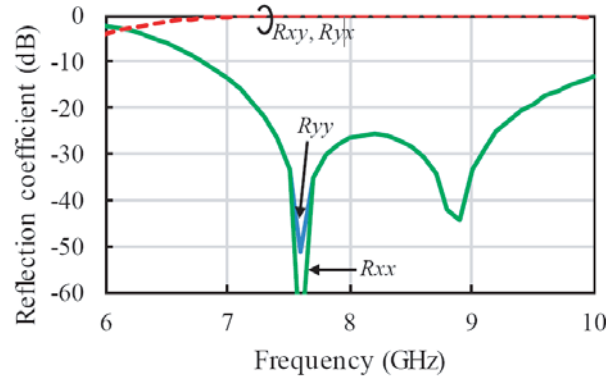**Figure 1.** Unit cell of MSPC with DSS patch element. The unit cell dimensions are 13.39 mm $\times$ 8.20 mm $\times$ 3.2 mm. p_s and p_l are optimized parameters. (a) Top and (b) side views.

**Figure 2.** Reflection coefficient of MSPC of infinite size.

which overlap by 1.18 mm. The unit cell is 13.39 mm (0.37λ at 8.5 GHz) in length, 8.20 mm (0.23λ) in width, and 3.2 mm (0.09λ) in thickness. The substrate is ROGERS RT/Duroid5880, for which the relative permittivity $\varepsilon_r = 2.2$ and $\tan \delta = 0.001$. In Fig. 1, the x and y axes are at $45°$ with respect to the sides of the unit cell and parallel to the two sides that form the right angles of the square elements.

Simulations were carried out using HFSS 17.0. Fig. 2 shows the reflection coefficient characteristics of the unit cell surrounded by periodic boundary conditions in the HFSS. R_{yx} is the reflection polarization of Y-polarization converted from an X-polarized incident wave from the plane wave port. For X- and Y-polarized incident waves, the reflection performance is almost identical. As shown, the Y-polarized wave is mainly reflected in a bandwidth of 32.4% (7.03 to 9.75 GHz), where the isolation between X- and Y-polarizations is more than 15 dB. The polarization conversion efficiency is more than 97% for orthogonal Y-polarization in this wide bandwidth.

3. MECHANISM OF POLARIZATION CONVERSION

The mechanism of polarization conversion with the structure of a DSS patch and a BC is discussed below. Figs. 3(a) and 3(b) show the current distributions on the DSS patch and BC at 7.6 GHz, respectively. In each figure, relative phase referencing the status of the upper figure is shown. Fig. 3(a) shows the current distribution on the patches at $0°$ and $90°$ radiating elliptical polarizations (EPs) at a high AR of around 10 dB. The current at $0°$ is weak, and that at $90°$ is strong, indicating that the EP
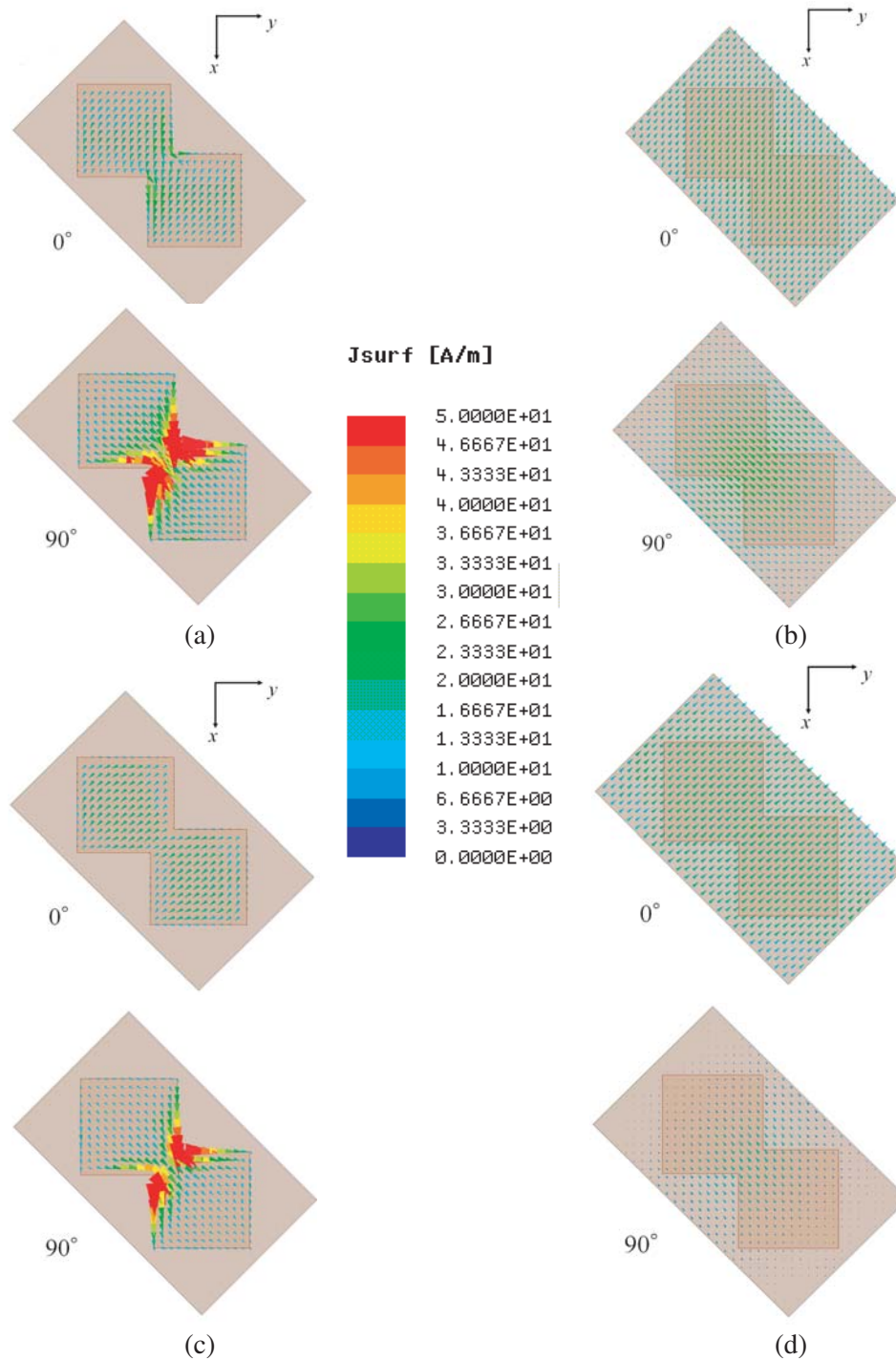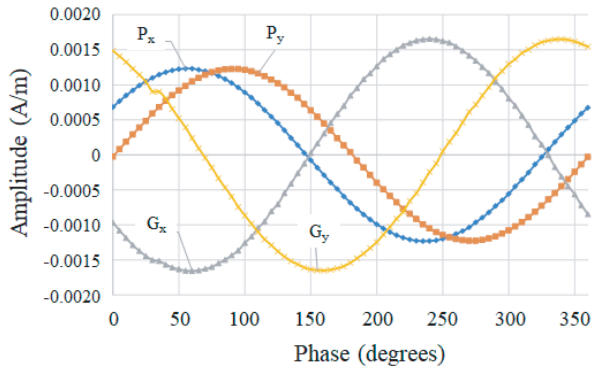
Figure 3. Current distributions on (a) DSS patch and (b) BC at 7.6 GHz and (c) DSS patch and (d) BC at 8.9 GHz for X-polarized incident wave.

is generated with the major axis parallel to the longer side of the unit cell. The current on the patch is easily focused around the narrow part of the patch as shown in Fig. 3(a). Fig. 3(b) shows the current distribution on the BC at 7.6 GHz. The current rotates counterclockwise with a very low AR, unlike in Fig. 3(a). This phenomenon is related to the DSS patch acting like a modified circularly polarized patch antenna with two truncated corners. Furthermore, the EP generated from the DSS patch is converted
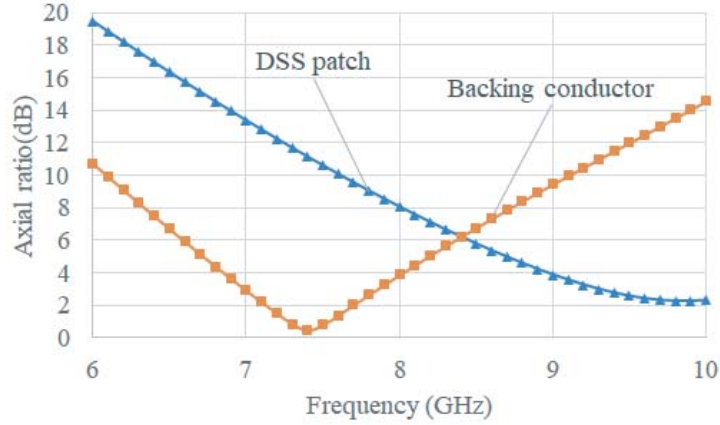
Figure 4. AR of radiation from DSS patch and BC for X-polarized incident wave.

Figure 5. Integrated values of current distribution on DSS patch and BC at 7.6 GHz.
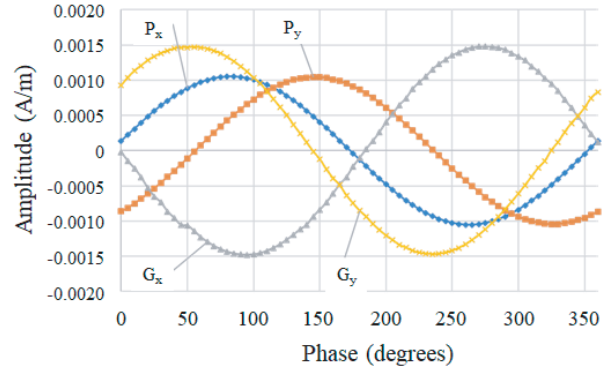
Figure 6. Integrated values of current distribution on DSS patch and BC at 8.9 GHz.

to CP due to the effect of the BC. Figs. 3(c) and 3(d) also show the current distributions on the DSS patch and BC, respectively, at 8.9 GHz.

The polarization conversion mechanism can be explained by the current behavior simulated using the face list in HFSS. In this analysis, current distribution on a selected part of DSS (both faces) or BC is transformed independently into the respective radiation far-field. Essentially the same technique with FDTD (Finite difference time domain) method has been used in [23] for analyzing the behavior of a low-profile spiral antenna using a metasurface. The AR characteristics of waves from both parts can be described as shown in Fig. 4. At 7.6 GHz, the DSS patch radiates LP-like polarization with a high AR of around 10 dB, and the BC radiates CP-like polarization with a low AR of around 1 dB. At 8.9 GHz, the DSS patch radiates EP with a low AR of 4 dB, and the BC radiates EP with a high AR of 9 dB. Unlike the case at 7.6 GHz, the DSS patch with a low AR of less than 4 dB radiates CP-like polarization, and the BC radiates LP-like polarization, namely EP with an AR of around 10 dB.

Figure 5 shows the results for the surface integrals of current over the DSS patch and the BC in the unit cell at 7.6 GHz, where P_x and G_x (P_y and G_y) are the $x(y)$ components of the integrated current on the DSS patch and the BC, respectively. The results confirm the following polarization conversion mechanism:

1. The DSS patch directly radiates the reflected wave of LP with P_x and P_y in-phase towards the $+z$ direction.

2. CP with G_x and G_y is reflected by the BC.

3. P_x and G_x towards $+z$ are cancelled out because their phase difference is π. This is because P_x

towards $-z$ is reflected as G_x with a phase shift of π.

4. P_y and G_y remain and form Y-polarized LP because they are not anti-phase.

The results for the integrals for 8.9 GHz are shown in Fig. 6. Low-AR EP is radiated from the DSS patch and high-AR EP radiated from the BC because the phase differences between the X and Y components are around 75° and 150°, respectively.

The behavior of the reflected wave for an X-polarized incident wave can be expressed as follows:

$$
\begin{aligned}
\mathbf{E} =& \mathbf{E}^{DSS} + \mathbf{E}^{BC} \\
=& |E_{x1}| \left\{ \hat{x}\, |P_x|\, e^{-j(kz+\phi_{Px})} + \hat{y}\, |P_y|\, e^{-j\left(kz+\phi_{Py}\right)} \right\} \\
& + (|E_{x0}| - |E_{x1}|) \left\{ \hat{x}\, |G_x|\, e^{-j(kz+\phi_{Gx})-j2kt} + \hat{y}\, |G_y|\, e^{-j\left(kz+\phi_{Gy}\right)-j2kt} \right\} \\
=& |E_{x0}| \left\{ \hat{x}\, (P_x + G_x) + \hat{y}\, (P_y + G_y) \right\} = |E_{x0}| \left(\hat{x} R_{xx} + \hat{y} R_{yx} \right)
\end{aligned}
\tag{1}
$$

where $\mathbf{E}^{DSS}$ is the electric field reflected by the current on the DSS patch and the diffracted wave from the current behind the DSS patch; $\mathbf{E}^{BC}$ is the electric field reflected by the BC; and k is the wavenumber. Furthermore, $|E_{x0}|$ is the amplitude of the X-polarized incident wave at $z = 0$ as long as no loss is assumed, and $|E_{x1}|$ and $|E_{x0}| - |E_{x1}|$ are amplitudes of the illuminated electric field to the DSS and BC, respectively. Here, Eq. (1) implies that $|E_{x1}|\,|P_x|$ and $(|E_{x0}| - |E_{x1}|)\,|G_x|$ should have the same amplitude in order to make the conversion available. For converting X-polarization to Y-polarization, $|P_x| = |G_x|$ and $\varphi_{Px} = \varphi_{Gx}$ are the required conditions. On the other hand, if both x and y components of the incident wave are considered, Eq. (1) can be extended to the following equation:

$$
\mathbf{E} = \begin{bmatrix} E_x \\ E_y \end{bmatrix} = \begin{bmatrix} R_{xx} & R_{xy} \\ R_{yx} & R_{yy} \end{bmatrix} \begin{bmatrix} |E_{x0}| \\ |E_{y0}| \end{bmatrix}.
\tag{2}
$$

Considering the symmetrical structure in Fig. 1 and the results in Fig. 2, $R_{xx} = R_{yy}$ and $R_{yx} = R_{xy}$ can be considered in Eq. (2) as far as the materials are isotropic.
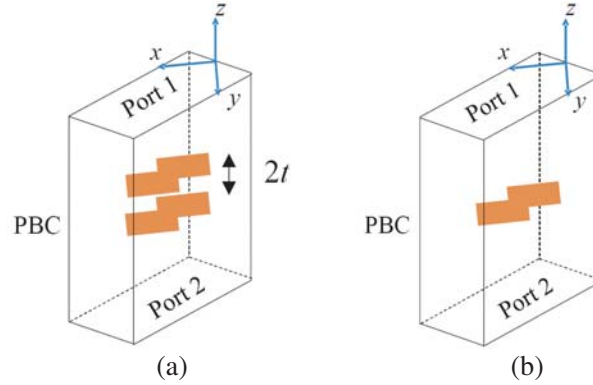
Figure 7. Additional models. (a) Double-layer model and (b) single-layer model. PBC: periodic boundary conditions.

To consider the mechanism using the above equations, two additional models, shown in Fig. 7, are used to evaluate $\mathbf{E}^{DSS}$ and $\mathbf{E}^{BC}$ separately. For this purpose, we consider the following parameters for Eq. (1):

$$
P_x = |P_x|\, e^{-j(kz+\phi_{Px})}
\tag{3}
$$

$$
G_x = |G_x|\, e^{-j(kz+\phi_{Gx})-2kt} e^{j\pi} = G'_x e^{j\pi}
\tag{4}
$$

$$
P_y = |P_y|\, e^{-j\left(kz+\phi_{Py}\right)}
\tag{5}
$$

$$
G_y = |G_y|\, e^{-j\left(kz+\phi_{Gy}\right)-2kt} e^{j\pi} = G'_y e^{j\pi}
\tag{6}
$$

where ϕ_{Px} is the phase shift of the x component from the X-polarized incident wave at the DSS patch; ϕ_{Gx} is the phase shift of the y component of the transmitted wave from the X-polarized incident wave

at the BC; and $e^{j\pi}$ is the phase shift caused by the reflection by the BC. In the models in Figs. 7(a) and 7(b), the unit cells are surrounded by periodic boundary conditions in HFSS. The incident wave is an X-polarized plane wave. The reflected waves from Port 1 to Port 1 in Fig. 7 (S_{11}) are assumed to be $\mathbf{E}^{\text{DSS}}$, and the transmitted wave from Port 1 to Port 2 (S_{21}) is assumed to be $\mathbf{E}^{\text{BC}}$. Therefore, G'_x and G'_y are the x and y components of the transmitted wave, respectively. In the practical structure in Fig. 1, the phase shift by π at the reflection at the BC is considered for evaluating G_x and G_y. The substrate is placed between the two patches in Fig. 7(a) with twice the thickness ($2t = 6.4\,\text{mm}$) shown in Fig. 1 considering the imaging situation with respect to the BC. Furthermore, the phase shifts between the ports and the DSS patches are excluded in this model.

As shown in Fig. 8(a), $|P_x|$ and $|P_y|$ are reflected with a magnitude of $6\,\text{dB}$ towards the incident wave. The magnitudes of $|G_x|$ and $|G_y|$ in Fig. 8(c) are around $-6\,\text{dB}$ ($|P_x| = |G_x|$). Therefore, the transmitted and reflected coefficients for both components are identical in this bandwidth. Considering the mechanism and the fact that the X-polarization is converted to Y-polarization, we can understand that this fact implies $|E_{x1}| = |E_{x0}| - |E_{x1}|$ (i.e., $|E_{x1}| = |E_{x0}|/2$) in Eq. (1). On the other hand, φ_{Px} and φ_{Gx} are almost constant at around $-135°$ ($\varphi_{Px} = \varphi_{Gx}$), covering a wideband frequency from 6.5 to $10\,\text{GHz}$. This explains why the proposed structure performs wideband polarization conversion. In the practical structure, the transmitted wave G'_x is reflected by the BC with a π phase shift, becoming G_x. Therefore, the X-polarization is cancelled in this structure in a wide band; only the y component (P_y and G_y) is reflected with a phase shift.
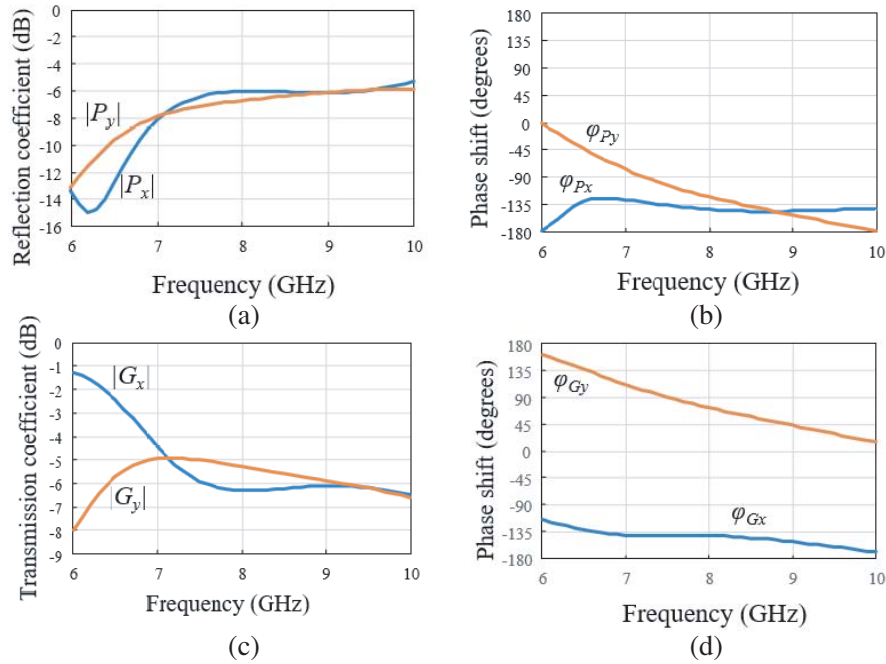
Figure 8. Characteristics of transmitted and reflected waves in Fig. 7 for X-polarized incident wave. (a) Reflection coefficient and (b) phase shift versus frequency for reflected waves. (c) Transmission coefficient and (d) phase shift versus frequency for transmitted waves.

Note that the coupling between the two DSS patches or between the DSS patch and the BC contributes to the transmission and the phase shift shown in Figs. 8(b) and 8(d), resulting in polarization conversion. In other words, P_x and P_y are almost in phase resulting in LP, and G_x and G_y are EP or CP, which contributes to making $|P_x| = |G_x|$, according to the phase characteristics in Fig. 8. Therefore, G_x and G_y are perturbed based on the principle of high-Q CP microstrip antennas with perturbed elements. The results in Fig. 8 support the discussions for Figs. 4–6; however, the frequency for the minimum ARs is slightly shifted because the edge effect is different between the structures in Figs. 1 and 7. For the case of a single-layer DSS patch, Fig. 9 shows that the X-polarized incident wave is mainly
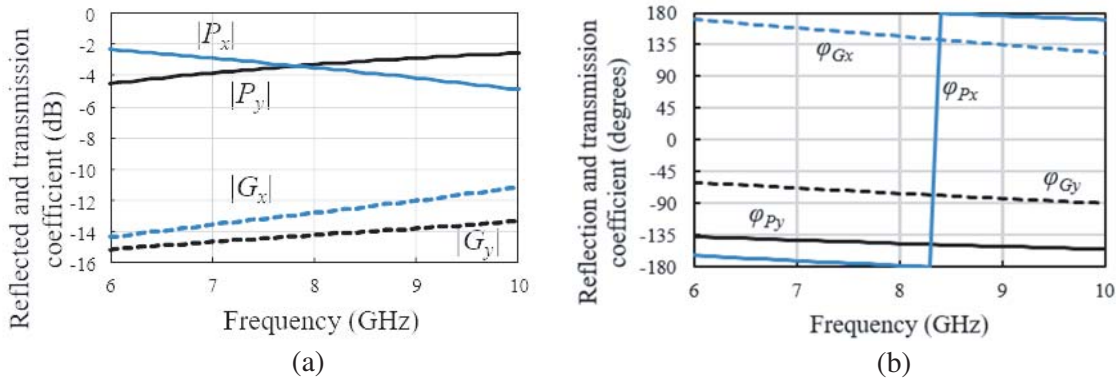
Figure 9. Characteristics of transmitted and reflected waves in Fig. 7(b) for X-polarized incident wave. (a) Amplitude and (b) phase characteristics.

reflected as EP (P_x and P_y) with phase differences of less than 45°, and the transmitted wave is EP, but its amplitude is less than -10 dB. The coupling between the DSS patch and BC thus contributes to polarization conversion.

4. PARAMETER STUDIES

To obtain the broadband characteristics discussed in Section 3, the effect of the joint size P_s on the isolation characteristics for the X-polarized incident wave is evaluated in this section.

Figure 10 shows the reflection coefficient of the normalized X-polarization by Y-polarization with respect to joint size P_s in Fig. 1. For $P_s = 0.98$ or 1.18 mm, there are two minima at different frequencies. With an increase in P_s, the two frequencies at the minima get closer to each other resulting in a narrower isolation bandwidth; however, the isolation between the X- and Y-polarizations can be increased. There is a trade-off between the bandwidth and the degree of isolation. $P_s = 1.18$ mm is obtained as the optimal parameter with 15-dB isolation.
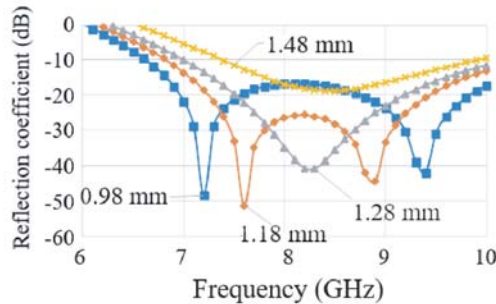

**Figure 10.** Variation in normalized reflection coefficient characteristics for X-polarization with P_s.

The results in Fig. 4 can be explained by the ARs of the radiation from the DSS patch and BC. Fig. 11 shows the variation in the ARs of radiation from the DSS patch and BC with P_s. With an increase in P_s, the frequencies for the best ARs of radiation from the DSS patch and BC get closer. The polarization conversion performance is thus improved at the center frequency. However, because the frequency for the best AR is decreased, there is an optimal value of $P_s (= 1.18$ mm) for the widest 15 dB isolation bandwidth.

The substrate thickness t is also an important factor. For obtaining the polarization conversion, the reflected wave from the DSS should be LP at 45°, and that from the BC should be close to CP. For the X-polarized incident wave, the condition of $|P_x| = |G_x|$, and $\varphi_{Px} = \varphi_{Gx}$ should be kept at the same

time. Fig. 12 shows characteristics of transmitted and reflected waves in Fig. 7 for the X-polarized incident wave when $t = 1.6$ mm and 4.8 mm. For $t = 1.6$ mm, this condition is satisfied only at 7.7 GHz according to Figs. 12(a) and 12(b). This is because the DSS with the BC has a high-Q value resulting in narrowband conversion characteristics with complicated amplitude and phase characteristics.
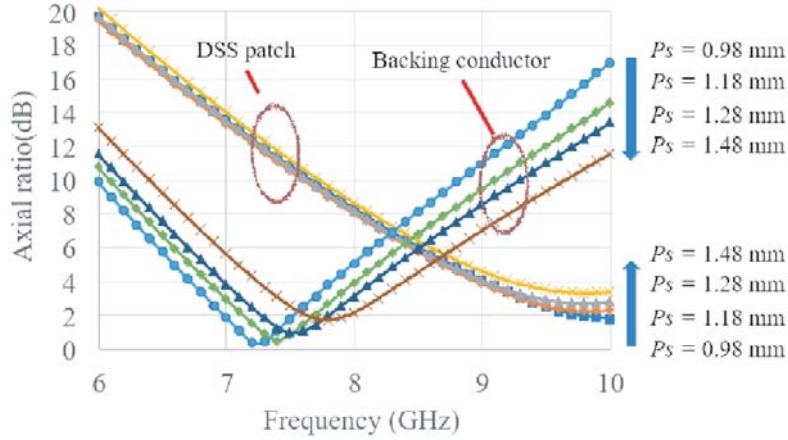
Figure 11. Variation in AR of radiation from DSS patch and BC with P_s.
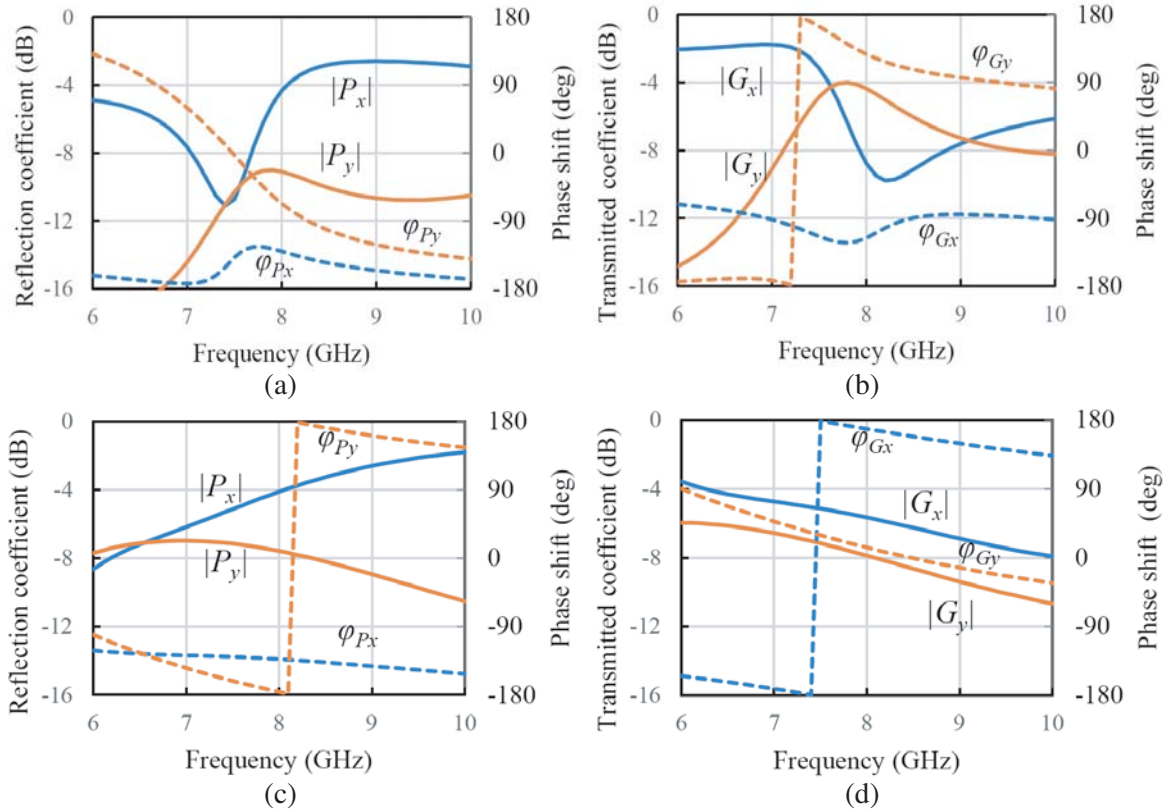
Figure 12. Characteristics of transmitted and reflected waves in Fig. 7 for X-polarized incident wave. (a) Reflection coefficient and phase shift for $t = 1.6$ mm, (b) Transmission coefficient and phase shift for $t = 1.6$ mm, (c) Reflection coefficient and phase shift for $t = 4.8$ mm and (d) Transmission coefficient and phase shift for $t = 4.8$ mm.

On the other hand, for $t = 4.8$ mm, φ_{Gx} is a little different from φ_{Px} by around $45°$ as shown in Fig. 12(c) and 12(d) because the kt gives a significant effect to the phase difference. Furthermore, the reflected wave by the BC is nearly X-polarized because $|P_y|$ and $|G_y|$ are smaller than $|P_x|$ and $|G_x|$, respectively. However, it is interesting that the amplitude difference between $|G_x|$ and $|G_y|$ and the phase difference between φ_{Px} and φ_{Gx} are almost constant with respect to frequency covering a wide bandwidth.

From the discussions with Figs. 8, 9, and 12, it can be concluded that $t = 3.2$ mm is a preferable value as far as the proposed DSS structure with the dimensions in Fig. 1 is used. Considering these characteristics in Fig. 12, amplitude and phase characteristics using a modified design of DSS should be controlled for enhancing the bandwidth with a larger t.

5. PERFORMANCE OF MSPC OF FINITE SIZE

5.1. Simulated Characteristics of MSPC

Figure 13 shows a photograph of a finite MSPC with the same unit cell as that shown in Fig. 2. In this MS structure, an 18×10 array of unit cells is arranged. Fig. 14 shows the simulated characteristics of the normalized reflection coefficient for the X-polarized wave compared to the Y-polarized wave when an X-polarized plane wave is incident. It can be seen that the X-polarized wave is suppressed, and the Y-polarized wave is mainly reflected, with an isolation of more than 15 dB at the center frequency in the fractional bandwidth of 35.2% (6.8 to 9.7 GHz). The results in Fig. 14 are close to those for the MSPC of infinite size in Fig. 2, although the magnitude of isolation in Fig. 14 for the finite structure is smaller than that for the MSPC of infinite size.

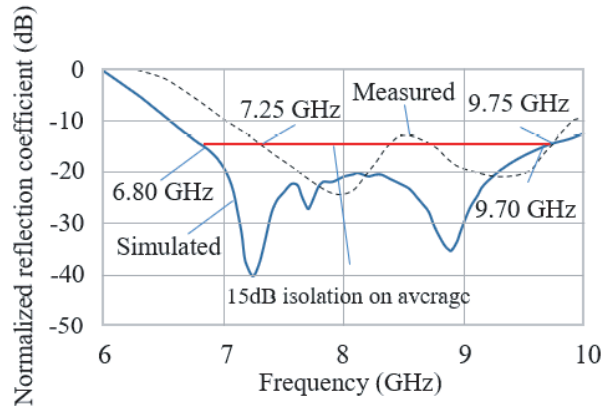**Figure 13.** Photograph of 18×10 array model.

Figure 14. Simulated and measured normalized reflection coefficient for X-polarization by Y-polarization in 18×10 array model.

5.2. Measured Characteristics of MSPC

The polarization conversion characteristics of the 18×10 array model were measured in an anechoic chamber. The measurement was carried out with a setup in Fig. 15 where a receiving double-ridge horn antenna (9 dBi) was installed 3.5 m away from the MSPC as shown in Fig. 15(a), and a transmitting antenna (5 dBi) with 0-dBm input power was an X-polarized wideband waveguide antenna installed 0.2 m away from the MSPC to keep sufficient reflected power density as shown in Fig. 15(b). This setup in Fig. 15(c) used a 26-dB low-noise amplifier around the receiving antenna to keep a sufficient signal-to-noise ratio at the receiver (a network analyzer). The polarization at the receiving antenna was changed by turning the antenna by $90°$. After confirming that the reflection coefficients for the X-polarization and Y-polarization from the same shape of a copper plate were identical, we obtained the reflection coefficient of the MSPC for both types of polarization.
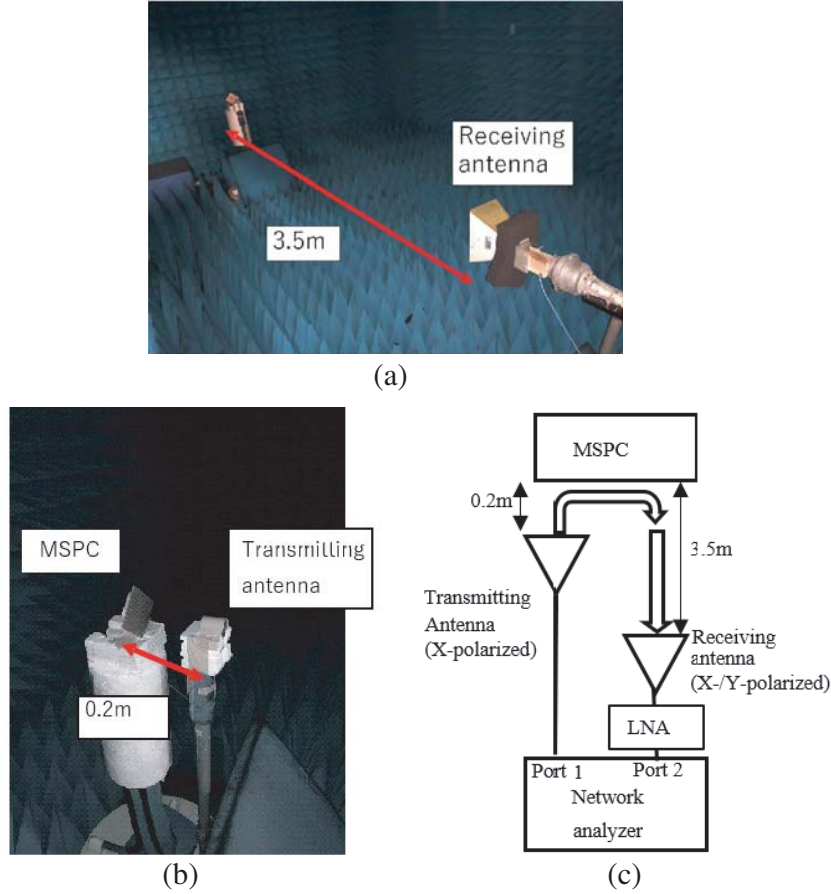
Figure 15. Experimental set up. (a) Receiving antenna, (b) transmitting antenna and (c) measurement system.

In Fig. 14, for evaluating the performance of the MSPC, the normalized measured reflection coefficient is obtained and shown for X-polarization compared to Y-polarization when the incident wave is X-polarized. Isolation around 15 dB is achieved in the frequency range of 7.25 to 9.75 GHz which is similar to the range in the simulation, but there is a frequency shift. This frequency shift and lower isolation are probably caused by the incident wave radiated by the transmitting antenna being relatively close to a spherical wave, whereas the incident wave in the simulation was a plane wave.

6. CONCLUSION

This study proposes a reflector principle that converts polarization by combining radiation from a perturbed DSS element and a BC. The merit of the proposed structure is a simple structure which has only one patch layer and one BC layer. The principle of the proposed polarization conversion, which is very simple, is based on synthesizing the polarization from the DSS and that from the BC in a wide frequency range. We have discussed the principle of wideband polarization conversion to cross polarization. To enhance the bandwidth, we can apply various wideband CP antenna design techniques for wideband polarization conversion [5, 6].

For the infinite periodic structure, 15 dB isolation (conversion efficiency: 97%) was observed between reflected X and Y polarization in a bandwidth of 35.2% (6.8 to 9.7 GHz). Similar performance was measured using a simple measurement setup (bandwidth of 29.4%; 7.25 to 9.75 GHz). The small discrepancy is caused by the transmitting antenna being close to the MSPC to keep a sufficient signal-to-noise ratio in the experiment. In future studies, we will improve this drawback to handle spherical waves or oblique incidence, and further wideband conversion characteristics are expected.

REFERENCES

1. Sievenpiper, D., L. Zhang, R. F. J. Broas, N. G. Alexopolous, and E. Yablonovitch, "High-impedance electromagnetic surfaces with a forbidden frequency band," *IEEE Transactions on Microwave Theory and Techniques*, Vol. 47, No. 11, 2059–2074, 1999.

2. Carrubba, E., S. Genovesi, A. Monorchio, G. Manara, "AMC-based low profile antennas for 4G communication services," *2007 IEEE Antennas and Propagation Society International Symposium*, 3364–3367, Honolulu, USA, Jun. 2007.

3. Qu, D., L. Shafai, and A. Foroozesh, "Improving microstrip patch antenna performance using EBG substrates," *IEE Proc.-Microw. Antennas Propag.*, Vol. 153, No. 6, 558–563, Dec. 2006.

4. Foroozesh, A. and L. Shafai, "Investigation into the application of artificial magnetic conductors to bandwidth broadening, gain enhancement and beam shaping of low profile and conventional monopole antennas," *IEEE Transactions on Antennas and Propagation*, Vol. 59, No. 1, 4–19, Jan. 2011.

5. Nakamura, T. and T. Fukusako, "Broadband design of circularly polarized microstrip patch antenna using artificial ground structure with rectangular unit cells," *IEEE Transactions on Antennas and Propagation*, Vol. 59, No. 6, 2103–2110, Jun. 2011.

6. Maruyama, S. and T. Fukusako, "An interpretative study on circularly polarized patch antenna using artificial ground structure," *IEEE Transactions on Antennas and Propagation*, Vol. 62, No. 11, 5919–5924, Nov. 2014.

7. Yang, F. and Y. Rahmat-Samii, "A low profile single dipole antenna radiating circularly polarized waves," *IEEE Transactions on Antennas and Propagation*, Vol. 53, No. 9, 3083–3086, Sep. 2005.

8. Ta, S. X. and I. Park, "Artificial magnetic conductor-based circularly polarized crossed-dipole antennas: 1. AMC structure with grounding pins," *Radio Science*, 630–641, May 2017.

9. Gao, X., X. Han, W.-P. Cao, H. O. Li, H. F. Ma, and T. J. Cui, "Ultrawideband and high-efficiency linear polarization converter based on double V-shaped metasurface," *IEEE Transactions on Antennas and Propagation*, Vol. 63, No. 8, 3522–3530, Aug. 2015.

10. Zheng, Q., C. Guo, and J. Ding, "Wideband metasurface-based reflective polarization converter for linear-to-linear and linear-to-circular polarization conversion," *IEEE Transactions on Antennas and Propagation*, Vol. 17, No. 8, 1459–1463, Aug. 2018.

11. Xu, H. X., S. W. Tang, G. M. Wang, T. Cai, W. Huang, Q. He, S. Sun, and L. Zhou, "Multifunctional microstrip array combining a linear polarizer and focusing metasurface," *IEEE Transactions on Antennas and Propagation*, Vol. 64, No. 8, 3676–3682, 2016.

12. Zhao, J. C. and Y. Z. Cheng, "A high-efficiency and broadband reflective 90° linear polarization rotator based on anisotropic metamaterial," *Applied Physics B*, Vol. 122, 255, 2016.

13. Zhao, J. C. and Y. Z. Cheng, "Ultrathin dual-band polarization angle independent 90° polarization rotator with giant optical activity based on planar chiral metamaterial," *Applied Physics B*, Vol. 124, 185, 2018.

14. Cheng, Y. Z., W. Li, and X. Mao, "Triple-band polarization angle independent 90° polarization rotator based on fermat's spiral structure planar chiral metamaterial," *Progress In Electromagnetics Research*, Vol. 165, 35–45, 2019.

15. Xu, H. X., G. W. Hu, L. Han, M. H. Jiang, Y. J. Huang, Y. Li, X. M. Yang, X. H Ling, L. Z. Chen, J. L. Zhao, and C. W. Qiu, "Chirality]assisted high]efficiency metasurfaces with independent control of phase, amplitude, and polarization," *Advanced Optical Materials*, Vol. 7, No. 4, 1801479, Feb. 2019.

16. Euler, M., V. Fusco, R. Cahill, and R. Dickie, "325 GHz single layer sub-millimeter wave FSS based split slot ring linear to circular polarization convertor," *IEEE Transactions on Antennas and Propagation*, Vol. 58, No. 7, 2457–2459, Jul. 2010.

17. Hwang, K. C., "A novel meander-grooved polarization twist reflector," *IEEE Microw. Wireless Compon. Lett.*, Vol. 20, No. 4, 217–219, Apr. 2010.

18. Zhu, X. C., et al., "A novel reflective surface with polarization rotation haracteristic," *IEEE Antennas Wireless Propag. Lett.*, Vol. 12, 968–971, Aug. 2013.

19. Chen, H., et al., "Ultra-wideband polarization conversion metasurfaces," *Proc. IEEE 3rd Asia Pac. Conf. Antennas Propag. (APCAP)*, 1009–1011, Jul. 2014.

20. Zhang, L., P. Zhou, H. Lu, H. Cheng, J. Xie, and L. Deng, "Ultra-thin effective metamaterial polarization rotator based on multiple plasmon resonances," *IEEE Antennas Wireless Propag. Lett.*, Vol. 14, 1157–1160, May 2015.

21. Li, L., Y. J. Li, Z. Wu, F. F. Huo, Y. L. Zhang, and C. S. Zhao, "Novel polarization reconfigurable converter based on multilayer frequency-selective surfaces," *Proc. IEEE*, Vol. 103, No. 7, 1057–1070, Jul. 2015.

22. Li, L., Y. Li, Z. Wu, F. Huo, Y. Zhang, and C. Zhao, "Novel polarization reconfigurable converter based on multilayer frequency-selective surfaces," *Proc. IEEE*, Vol. 103, No. 7, 1057–1070, Jul. 2015.

23. Nakano, H., K. Kikkawa, N. Kondo, Y. Iitsuka, and J. Yamauchi, "Low-profile equiangular spiral antenna backed by an EBG reflector," *IEEE Transactions on Antennas and Propagation*, Vol. 57, No. 5, 1309–1318, May 2009.